Characterization of saline aqueous solutions upwelling under Ceres' surface: a focus on chemical equilibria in the H2O-CO2-NaCl supply ascent system

Maria PEDONE[1], Eleonora Ammannito[2], Christina Plainaki[2], Maria Cristina De Sanctis[3], Andrea Raponi[4], Simone De Angelis[5], Mauro Ciarniello[4], Marco Ferrari[4], Alessandro Frigeri[6], and Filippo Giacomo Carrozzo[3]

[1]ASI (Italian Space Agency)
[2]Agenzia Spaziale Italiana
[3]INAF
[4]National Institute for Astrophysics
[5]Unknown
[6]Istituto Nazionale di Astrofisica

November 24, 2022

Abstract

In Ceres dwarf planet, a portion of a prior ocean at shallow depth may still exist today as localized reservoirs. In this work, we constrained chemical and geophysical properties of initial aqueous fluids, characterizing the reservoirs, located under two selected craters: Kupalo and Juling. At first, we applied FREZCHEM code to simulate brines' freezing processes, under different values of initial total pressure in which the starting solutions have cooled to precipitate the solids characterizing these craters. Then, we compared the results with our chemical equilibria calculations to understand the equilibrium state for each precipitated mineral, during the cooling process, related to the activities of solutes and the ionic strength of solutions. Decreasing temperature caused the precipitations of carbonates (thermodynamically favored), followed by the formation of sulphates and, later, of Cl-bearing salts from more saline brines. Solids precipitation feeds cooling process, changing the velocity/density ratios of aqueous solutions that would have arrived at surface erupting with a velocity of 8·10-5 m/s. An excess of pressure in the reservoirs could have supported an intrusion of briny materials to surface, and, in our simulations, we suggest that sodium-salts formation is pressure-dependent. This supports the hypothesis that different "cooling chambers", at different pressure conditions, may exist under the craters. Moreover, beneath Kupalo, at specific pressure condition, some kinetics-dependent molecules could form, suggesting that aqueous solutions plausibly were affected by kinetics slower than the nearby Juling.

Characterization of saline aqueous solutions upwelling under Ceres' surface: a focus on chemical equilibria in the H_2O-CO_2-NaCl supply ascent system

M. Pedone[1*], E. Ammannito[1], C. Plainaki[1], M. C. De Sanctis[2], A. Raponi[2], S. De Angelis[2], M. Ciarniello[2], M. Ferrari[2], A. Frigeri[2] and F. G. Carrozzo[2]

[1]ASI, Agenzia Spaziale Italiana, via del Politecnico s.n.c, 00133, Rome, Italy.

[2]IAPS, Istituto di Astrofisica e Planetologia Spaziali, INAF, Via del Fosso del Cavaliere, 100, 00133, Rome, Italy.

*Corresponding author: Maria Pedone (maria.pedone@est.asi.it)

Key Points:

- Carbonates and salts-rich material reached Ceres' surface beneath Kupalo and Juling craters
- Some compositional differences suggest that the initial brines had different speciation and freezed at different T-P conditions
- Beneath Kupalo crater aqueous solutions were affected by slow kinetics, possibly, rising and cooling more slowly than Juling

Abstract

In Ceres dwarf planet, a portion of a prior ocean at shallow depth may still exist today as localized reservoirs. In this work, we constrained chemical and geophysical properties of initial aqueous fluids, characterizing the reservoirs, located under two selected craters: Kupalo and Juling.

At first, we applied FREZCHEM code to simulate brines' freezing processes, under different values of initial total pressure in which the starting solutions have cooled to precipitate the solids characterizing these craters. Then, we compared the results with our chemical equilibria calculations to understand the equilibrium state for each precipitated mineral, during the cooling process, related to the activities of solutes and the ionic strength of solutions. Decreasing temperature caused the precipitations of carbonates (thermodynamically favored), followed by the formation of sulphates and, later, of Cl-bearing salts from more saline brines. Solids precipitation feeds cooling process, changing the velocity/density ratios of aqueous solutions that would have arrived at surface erupting with a velocity of $\sim 8 \cdot 10^{-5}$ m/s.

An excess of pressure in the reservoirs could have supported an intrusion of briny materials to surface, and, in our simulations, we suggest that sodium-salts formation is pressure-dependent. This supports the hypothesis that different "cooling chambers", at different pressure conditions, may exist under the craters. Moreover, beneath Kupalo, at specific pressure condition, some kinetics-dependent molecules could form, suggesting that aqueous solutions plausibly were affected by kinetics slower than the nearby Juling.

Plain Language Summary

Cryovolcanism is a process that can occur on icy bodies that have fluids in their interior. The origin of Ceres' surface materials is still to be fully understood and here we investigate the possible mechanisms of ascending fluids on Ceres. Cold fluids like aqueous solutions could have risen to the surface and, here, we try to characterize the properties of the ancient water body, from a chemical and physical point of view, to understand Ceres' history.

1 Introduction

In the Solar System, Ceres is the closest to the Sun among the icy-bodies known to possess a substantial (>10 wt.%) ice fraction (Neveu and Desch, 2015). Several studies showed that Ceres contains about 25 wt.% water in form of ice and/or bound to minerals, as evidenced by its bulk density (Castillo-Rogez and McCord, 2010), indicating the presence of subsurface liquid water like Europa and Enceladus (McCord and Sotin, 2005; Castillo-Rogez and McCord, 2010; Neveu et al., 2015). To explain density of Ceres' upper layer, Fu et al. (2017) invoked ≤25 vol.% water ice together with ≥36 vol.% gas and salt hydrates. Several authors (McCord and Sotin, 2005; Castillo-Rogez and McCord, 2010; Castillo-Rogez, 2011; Neveu et al., 2015; Hesse and Castillo-Rogez, 2019) have modelled Ceres as having a rocky core and pure ice mantle (ρ_m = 918 kg·m^{-3}) or ice containing solutes or clathrates (Castillo-Rogez and McCord, 2010). Recently, without invoking low-density phases, Zolotov (2020) modelled Ceres' bulk density (~2160 kg·m^{-3}; Park et al., 2019) by using mixtures of chondrites and insoluble organic matter, matching the NASA *Dawn* mission (Russell et al., 2016; Russell and Raymond, 2011) results. Ceres's surface is dark (geometric albedo 0.09-0.1) and relatively uniform (Li et al., 2006, 2019; Neveu

and Desch, 2015; Ciarniello et al., 2017), with spectra consistent with minerals resulting from aqueous alteration (Lebofsky et al., 1981; Rivkin et al., 2006; De Sanctis et al., 2016), possibly brucite, magnetite, carbonates, and phyllosilicates (King et al., 1992; Milliken and Rivkin, 2009; Rivkin et al., 2012; Beck et al., 2015; Ammannito et al., 2016; Thomas et al., 2019).

The NASA *Dawn* mission provided evidence of subsurface liquid delivery to the surface and precipitation of different mineralogical facies after dehydration/water depletion, confirmed by the presence, on Ceres' surface, of an assemblage of Mg-phyllosilicates, NH_4-bearing species, dark materials, and Mg-Ca carbonates (Carrozzo et al., 2018; De Sanctis et al., 2015). Moreover, Visible and InfraRed spectrometer's data (VIR, De Sanctis et al., 2011) suggested that a different style of aqueous alteration occurred locally (Carrozzo et al., 2018) and some differences in carbonate compositions. For example, the carbonate found in Occator, natrite (Na_2CO_3), is different from the Mg-Ca carbonate detected in the global Ceres spectrum, and it was not observed in Carbonaceous Chondrites (CC), generally considered as analogues of Ceres (De Sanctis et al., 2016; McSween et al., 2017). Natrite is found in terrestrial alkaline hydrothermal and evaporitic environments, and it has been also detected in Enceladus' plumes (Postberg et al., 2011), along with $NaHCO_3$ and NaCl.

The origin of Na carbonate on Ceres is debated. It is clear that some occurrences of Na_2CO_3 are related to geologically recently upwelled material from the subsurface, such as Occator's central dome and Ahuna Mons (De Sanctis et al., 2016; Zambon et al., 2017). Moreover, the presence of sodium carbonates was associated with domes and mounds although not exactly superimposed (Carrozzo et al., 2018). Na carbonate was also found in crater ejecta, rims, central peaks and floors, such as Kupalo and Haulani, or in small bright exposures, such as in Ikapati crater (Carrozzo et al., 2018). Morphologies, such as floor fractures, may be indicative of upwelling processes which occurred on Ceres induced by exogenous and/or endogenous causes, yet to be better defined and not necessarily exclusive (Thomas et al., 2019). Such kind of geological settings could support a subsurface aqueous origin of hydrated sodium carbonates that are delivered to the surface from ascending fluids and their partial decomposition/dehydration on surface airless environments.

To test this hypothesis, we studied a specific location on Ceres: the area of Kupalo and Juling craters. From recent structural analysis (Ruiz et al., 2019) the area of Kupalo and Juling is characterized by distinctive tectonics suggesting that endogenous processes have insisted on both craters.

These two geologically young craters host some of the brightest and most extensive sodium carbonates rich areas (Carrozzo et al., 2018; De Sanctis et al., 2019). The craters were selected in order to: i) understand the causes and processes that led to their surface compositions, and ii) to find a model for the evolution of the supply and ascent H_2O-CO_2-NaCl system.

Since hydrated ammonia salts, as NH_4Cl or NH_4HCO_3 are not found to form preferentially, with respect to sodium salts, even in ammonium-dominated solutions (Vu et al., 2017), we have deliberately neglected to investigate the role of ammonia dwelling on the main species in a saline aquifer.

Moreover, by using the FREZCHEM model (FREeZing CHEMistry, Marion et al., 2010 and references therein), for calculating the equilibrium composition of aqueous solutions at specified temperatures, for the first time, we will provide some clues about the path and time (not provided by the code, Marion and Grant, 1994) required to reach solids equilibrium states. For some solids, as explained in the main text, the equilibrium state could be highly dependent on kinetics and internal pressurization of feeding conduits.

106

107 1.1 Study area: morphologies and main spectral features

108 Juling (36° S, 168.3° E, D=20 km) and Kupalo (39.6° S, 173° E, D=26 km) craters display sharp
109 rims and well-preserved ejecta morphologies, as shown in Fig. 1, indicative of their young age
110 (Stein et al., 2019).
111

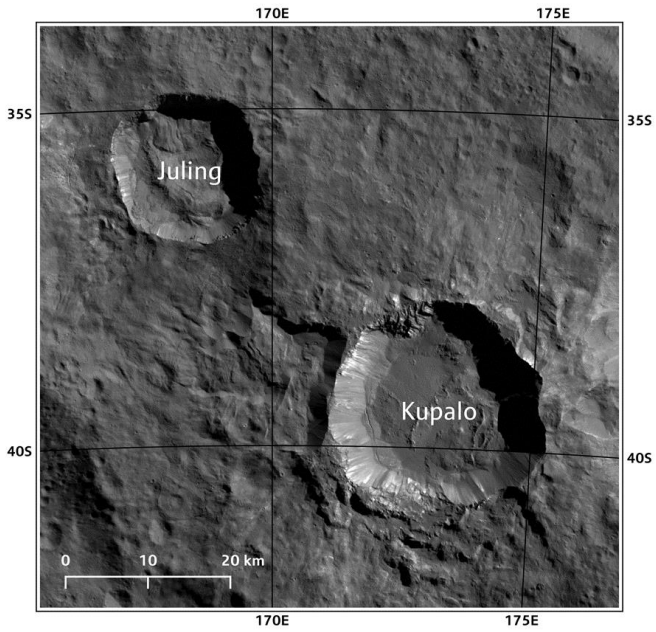

112
113 **Figure 1.** Context map of the study area with nomenclature and image mosaic (data from DLR).
114

115 The two craters contain extensive bright predominantly carbonates-bearing areas (rim/wall
116 faculae, Stein et al., 2019) and bright ejecta blankets. In Juling, the crater floor is not flat
117 showing flows traces seen suggestive of efficient material transport and the morphology
118 indicates presence of water ice (Raponi et al., 2018). Ice signature was observed in the northern
119 crater walls (Raponi et al., 2018), and areas with carbonates are present in the southern rim (De
120 Sanctis et al., 2019). Similar to the nearby Juling crater, a large amount of carbonates is present
121 in the Kupalo crater, showing bright ejecta and sharp rims with bright material exposures (De
122 Sanctis et al., 2019). Spectral analysis of Juling and Kupalo (De Sanctis et al., 2019) evidences
123 some substantial differences in the chemical composition of carbonates: Juling, as well as most
124 of Ceres, is rich in Ca-Mg carbonates, while Kupalo has mainly Na carbonate (Carrozzo et al.,
125 2018; Raponi et al., 2019).
126

127 1.2 Saline aqueous solutions' upwelling

128 As for the evaporative processes that occur on Earth, some authors (De Sanctis et al., 2016;
129 Nathues et al., 2017) suggested deposition of detected salts, including ammonium salts (as NH_4-

chloride, Raponi et al., 2019), and abundant Na_2CO_3, as the consequence of aqueous solution upwelling toward the surface.

Within Occator crater, in which Na_2CO_3 and NH_4-chloride were detected, calculations about chemical equilibria of brines showed that the initial solutions have not exceeded 273 K in temperature, 100 g per kg H_2O in the salinity and they had pH of ~10 (Zolotov, 2017).

Freezing models showed that solids precipitate increasing salinity and cooling of initial solutions. Since hydrated forms of carbonates and ammonium salts, as water ice (Fanale and Salvail, 1989; Hayne and Aharonson, 2015; Formisano et al., 2016), are not stable at Ceres' surface temperatures they decompose.

Natrite (Na_2CO_3) is the likely dehydration product of initially water-deposited carbonates, as further described below. Water-deposition of carbonates, through a process of evaporation/water depletion, led to the precipitation of hydrated Na carbonate (natron $Na_2CO_3 \cdot 10H_2O$). Precipitation of natron, then, led to enrich remaining brines in other more soluble solids, such as Na chloride, which is the most soluble salt in water (solubility of NaCl = 6.09 mole per kg H_2O, at 0° C; Zolotov, 2017).

In turn, high-solubility salts, as NaCl, the most predominant component in saline aquifers (Anabaraonye et al., 2019) could precipitate from more saline and colder solutions accumulated at later stages of aqueous activity, suggesting, in other words, the occurrence of the final phase of exsolution.

As well as on Earth, during the dehydration process, it is expected first the precipitation of less soluble solids (carbonates) and then the more soluble phases (sulphates and, finally, chlorides). At VIR resolution, no gypsum and other sulphates were actually observed at surface, and the apparent lack of sulphates in Ceres' surface salts supports its similarity with bodies of outer solar system (Zolotov, 2020). As regards chlorides, they were detected on Occator crater along with sodium bicarbonate ($NaHCO_3$), considered as possible constituents of Ceres' brines (Quick et al., 2019, and references therein).

The original reservoir configuration is debated (Quick et al., 2019), as well as the possibility of upwelling of material situated between the crust and mantle (Ermakov et al., 2017). At present, at limit of our knowledge, a partially crystallized briny reservoir may be exist (Hesse and Castillo-Rogez, 2019) containing concentrated salt species with densities ≥2000 kg/m^3 mixed with low-density cryomagmatic constituents as clathrates and ice (Quick et al., 2019). Resulting brines could be characterized by densities (1140 kg/m^3, calculated by Quick et al., 2019, below Occator) lower than crust density (1300 kg/m^3) and reach the surface.

Among ascent scenarios, listed by Ruesch et al. (2019), a decompression of ascending gas-rich ice has been also proposed as well (Zolotov, 2015; Nathues et al., 2017; Ruesch et al., 2017, 2019).

For the aforementioned open questions, freezing simulations are carried out to find clues about evolution history of Ceres dwarf planet.

2 Characterization of initial solutions

FREZCHEM was used to explore cold chemical processes in the Ceres' concentrated electrolyte solutions. The code is parameterized for concentrated electrolyte solutions using the Pitzer equations (Pitzer, 1995) for temperatures from <-70 to 25 °C, pressures from 1 to 1000 bars, and the system Na-K-Mg-Ca-Fe-H-Cl-SO_4-NO_3-OH-HCO_3-CO_3-CO_2-CH_4-H_2O (Marion and Grant, 1994; Marion et al., 2003).

For each crater, assuming the freezing process was P-T-dependent, we carried out three freezing simulations, decreasing temperatures from 273 K to 243 K at three selected initial values of total pressure (1, 1.5 and 3 bars).
In our calculations, the first step was to characterize the initial solutions compositions which, after cooling/precipitation processes, delivered salts which better can approximate the actual surface solid compositions found, by spectral analysis, in the Juling and Kupalo craters. In fact, the two craters, even if very close to each other, differ in the observed mineralogy as reported in table 1.

Table 1

This table lists the observed species in the two craters relevant for the simulations here reported

	Na carbonate	Mg, Ca carbonate	Water ice
Kupalo	abundant	yes	no
Juling	minor	yes	yes

Since abundant natrite was found in Kupalo but not in Juling (Carrozzo et al., 2018), and, assuming that the same reservoir may feed the adjacent craters, we explored the possibility to derive if the initial aqueous solutions beneath Kupalo and Juling had different speciation or suffered differentiation.

In the attempt to characterize the initial aqueous solutions of Kupalo and Juling, we started from the work of Zolotov (2017) that focused on bright salt deposits on Occator crater, rich in Na carbonate (De Sanctis et al., 2016; Raponi et al., 2019). Starting from a reservoir not exceeding 273 K in temperature, 100 g per kg of H_2O in the salinity and characterized by pH~10, Zolotov's (2017) freezing models revealed early precipitation of natron ($Na_2CO_3 \cdot 10H_2O$) followed by minor nahcolite ($NaHCO_3$). The author found that Occator's ice-free salt deposits formed through a post-depositional sublimation of ice followed by dehydration of $Na_2CO_3 \cdot 10H_2O$ and $NaHCO_3$ to Na_2CO_3.

We used as starting point the same physical conditions found in Zolotov (2017) and, then, after freezing simulations, we found the initial speciation of aqueous solutions under Kupalo and Juling (Tab. 2). Ionic species amount as the main cations sodium, calcium and magnesium (Na^+, Ca^{++} and Mg^{++}) are shown in table 2 and given in molal concentrations (mol/kg of water).
Chlorine (Cl^-, expressed in mol/kg, Tab. 2) and the carbonated species (CO_3^{--} and HCO_3^-) are the main negative ionic species deriving from the dissolved solids in the aqueous solution (NaCl and carbonates, respectively). In addition, carbonated ions also derive from the dissolution of $CO_{2\,(gas)}$ which forms the aqueous molecule H_2CO_3 that, such as an acid, after two dissociation processes, releases ionic forms: HCO_3^- and CO_3^{--}. Dissolved CO_2 is only a minor component for the alkaline nature of the solutions (Zolotov, 2017) and here we consider an initial CO_2 content of about $1.3\text{-}1.5 \cdot 10^{-5}$ mol/kg (Tab. 2) corresponding to a pressure of $3 \cdot 10^{-4}$ bars.
The total amount of $CO_3^{--}+HCO_3^-$ was initialized as equivalents/kg of water (Marion et al., 2010) so that the concentrations (in mol/kg) multiplied for the charge number ($2CO_3^{--}+HCO_3^-$) return alkalinity values (expressed as "Alk") ranging between 1.20-1.60 (in equivalents/kg), in line with literature (Zolotov, 2017).

The initial chemical compositions of Kupalo and Juling solutions are compared with Occator solutions (A, B, C given in Zolotov, 2017; see Tab. 2). In table 2, "Occator A" is the average composition, "Occator B" refers to the maximum reported abundance of Na_2CO_3 and "Occator C" represents the minimum abundance of Na_2CO_3.

The main difference between Kupalo, Juling (our work) and Occator (Zolotov, 2017) was found in chlorine and sodium contents.

For Juling crater's solutions, we excluded the case in which the sodium amount was about 1.4-1.8 (mol/kg) as in Occator (Tab. 2). In fact, by setting the initial Na^+ concentration at value ≥ 0.8 moles/kg of water, Juling's aqueous solutions freezing models led to (unreal) precipitation of gypsum (at T=273 K) and other sulphates for further steps of FREZCHEM code and no Ca and Mg-carbonates could be formed. For this reason, we reasonably consider that Juling was characterized by sodium-depleted solutions (Tab. 2).

Instead, in Kupalo solutions, chlorine and sodium amounts were calculated by adding about 10 mol.% NaCl to Juling-like solutions leading to high Na and Cl contents (1.8 and 0.1 mol/kg, respectively; see Tab. 2). To exclude the possibility that Kupalo solutions were chlorine-depleted (as nearby Juling) we also carried out the simulations with the initial amount of Juling (Cl=0.04 mol/kg), but, in that case, sodium-salts never formed under Kupalo surface. The lack of sodium-salts and sodium-carbonates is not in line with results derived from Carrozzo et al. (2018).

These results suggest that the initial aqueous solutions compositions under the selected craters differ for the availability of such species (e.g., higher chlorine and sodium amounts in Kupalo), in line with the large abundance of sodium compounds found in Kupalo and not in Juling (Carrozzo et al., 2018). Finally, not having many clues about potassium (K^+) and sulphate (SO_4^{--}) contents, we may hypothesize an initial concentration (K^+= 0.2 and SO_4^{--}= 0.1 mol/kg) so that the mass ratio (K^+:SO_4^{--}= 2:1) compensate the charge ratio (K^+:SO_4^{--}= 1:2).

The obtained solutions were electrically balanced in cations and anions (CB is the charge balance expressed as CB_+ and CB_-, respectively for cations and anions; Tab. 2).

Table 2

The initial speciation of aqueous solutions in this work (Kupalo and Juling) compared to Occator's data (A, B, C; given in Zolotov, 2017)

Crater	Cl^-	CO_2	Na^+	Ca^{++}	Mg^{++}	CB_+	CB_-	*IS*	*IS**	X	Y
Kupalo	0.10	$1.38 \cdot 10^{-5}$	1.80	0.89	0.80	2.00	2.10	2.05	2.98	42.80	30.45
Juling	0.04	$1.57 \cdot 10^{-5}$	0.20	0.89	0.80	2.05	1.94	1.99	2.02	44.96	11.67
Occator A	0.04	$8.74 \cdot 10^{-6}$	1.60					2.57		46.28	27.27
Occator B	0.01	$1.16 \cdot 10^{-6}$	1.80					2.72		47.08	28.57
Occator C	0.08	$3.63 \cdot 10^{-5}$	1.40					2.39		45.03	25.81

Note. In our simulations, the calculated equilibrium compositions refer to the water-salts system where the main chemical species are H_2O, CO_2, and NaCl.

Cl^-, Na^+, Ca^{++} and Mg^{++} are expressed in molal concentrations (i.e., moles/kg of water). CO_2 is gas dissolved in aqueous solutions and the concentrations given here (mol/kg) correspond to a pressure value of $3 \cdot 10^{-4}$ bars.

CB_+ and CB_- are positive and negative charge balance for given solutions, respectively. *IS* is the calculated ionic strength. *IS** is the average of ionic strength found in temperature values ranged between 273 K and 268 K. Finally, X and Y values, in the last two columns, were used to plot the Langelier-Ludwig diagram (1942) in Fig. 2. $X=50*(Alk)/(Alk+Cl^-+SO_4^{--})$ and $Y= 50*(Na^++K^+)/(Na^++K^++Ca^{++}+Mg^{++})$.

In the calculation of charge balance (CB) we have to consider that saline aqueous solutions are not exactly "ideal"; for this reason, we extrapolated the CB_+ and CB_- values (not exactly identical; see Tab. 2) starting from the activities of the *i*-ionic species (a_i), which are not the concentration values (c_i), as explained below. In detail, the positive charge balance (CB_+) and the negative charge balance (CB_-), in Tab. 2, were calculated by multiplying the ionic activities (a_i) for the charge square number (z^2) of ionic species. In this way, the ionic strength of solution (*IS*, expressed in mol/kg; Tab. 2 and Eq. 1) has the same formula as follows:

$$IS = \frac{1}{2}\sum_{i=1}^{N} a_i z_i^2$$

Eq. (1)

where the activities (a_i) of positive and negative *i*-ionic species are calculated multiplying the activity coefficient (γ) for concentration values (c_i) as follows:

$$a_i = \gamma c_i$$

Eq. (2)

Ionic strengths (*IS*) of solutions under Kupalo and Juling (~2 mol/kg) are close to Occator ionic strength values (Tab. 2). As explained in the next sessions of this work, *IS* values increase as aqueous solutions are cooled. For comparison, in Tab. 1 the average of ionic strength values between 273-268 K T-range (*IS**>*IS*) are reported.

In the same table, X and Y values (two last columns) were used to plot the solutions in the Langelier-Ludwig diagram (1942).

X and Y values were calculated starting from the amounts of the main ionic species which are divided into 4 groups: i) chlorine+sulphates; ii) alkaline metals (sodium+potassium); iii) alkaline-earth metals (calcium+magnesium); iv) carbonated species. For calculation of the amounts of the i), ii), and iii) groups, the concentration values (mol/kg) are used. Instead, for the group of carbonated species, the alkalinity value (Alk, in equivalents/kg) is requested.

Then, in Tab. 1 and Fig. 2, X and Y are given as follows:

$X=50*(Alk)/(Alk+Cl^-+SO_4^{--})$ Eq. (3)

$Y=50*(Na^++K^+)/(Na^++K^++Ca^{++}+Mg^{++})$ Eq. (4)

By a compositional point of view, the solutions in Kupalo and Juling reservoirs were characterized by the predominance of carbonated species ($HCO_3^- + CO_3^{--}$), but they differ for the alkaline/alkaline-earth contents, falling into two different quadrants (Fig. 2). Since the diagram consider the aqueous solutions only by a chemical point of view (anions/cations contents) excluding physical properties such as gravity, we can explore the possibility to see our given solutions in a broader perspective. If they were natural waters on Earth, they would be similar to bicarbonate-solutions with different metals contents falling in between three main terrestrial end-members.

In particular, the end-members are: i) Earth seawater-like solutions (chlorinated and sodium-enriched solutions; red star in Fig. 2); ii) Earth geothermal brines-like solutions (sulphate-chlorinated and sodium-enriched solutions); and iii) Earth cold groundwater-like solutions (bicarbonate and calcium-magnesium-enriched). Similarly to Earth, high carbonated species

297 contents suggest the interaction between Ceres' brines and CO_2 (the corresponding amounts were
298 summarized in Tab. 2).
299 Juling solutions are more like the Earth cold groundwater field (Fig. 2); instead, Kupalo
300 solutions, closer to Occator (Fig. 2), seems to be a mixture of Earth geothermal brines and cold
301 groundwater-like. Finally, it should be noted that Occator bright material actually has different
302 mineralogy with respect to Ceres average composition (Raponi et al., 2019) and, in the diagram,
303 it is in a different quadrant with respect to the one characterizing Juling (and Juling-like)
304 compositions. Juling composition, in terms of type of carbonate is more similar to the Ceres
305 average material, thus we can assume that also Ceres average can be in same quadrant of Juling
306 solutions.
307

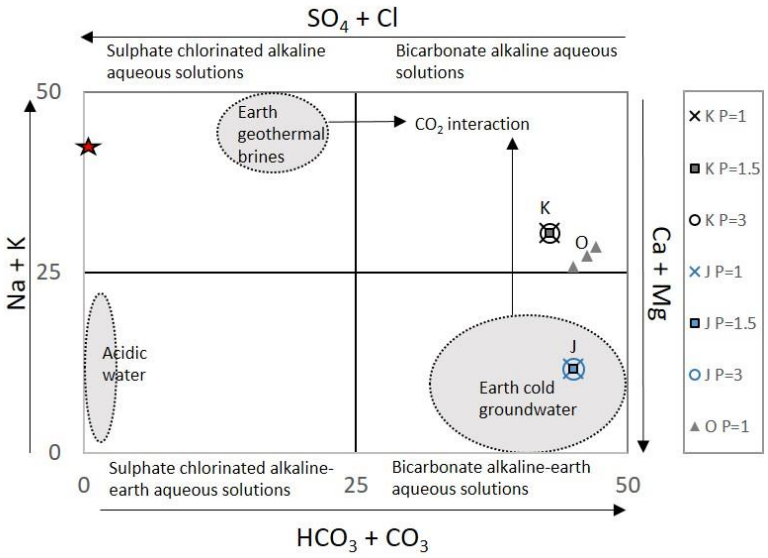

308
309
310 **Figure 2.** Langelier-Ludwig diagram (1942) showing Ceres' brines in comparison with the main
311 aqueous targets on Earth. From a chemical point of view (anions/cations contents), we explore
312 the possibility to see our given solutions in a broader perspective (see text) by plotting the target
313 solutions inside specific quadrants that characterize chemical properties of natural water on
314 Earth. In detail, the fields of the acidic water, geothermal brines, and cold groundwater are given.
315 Earth seawater, characterized by conservative behaviour of the main ionic species, is plotted as
316 unique point (red star). By a compositional point of view, Ceres' brines are characterized by the
317 predominance of bicarbonate ion (HCO_3), but they differ for the alkaline/alkaline-earth contents
318 (Na+K and Ca+Mg, respectively). The diagram is created from dataset shown in Tab. 2. Kupalo
319 (K) and Juling (J) solutions are given at total pressure values (P) of 1, 1.5 and 3 bars (see
320 legend). O: Occator solutions (grey triangles) are taken from Zolotov, 2017 (A, B and C at P=1
321 bar).
322

323 2.1 FREZCHEM code applied to freezing process

324 Freezing processes occurred in our initial aqueous solutions characterizing Ceres' Kupalo and
325 Juling craters were simulated by using FREZCHEM fractional crystallization pathway by
326 changing temperature value (in Kelvin) from the initial T_i=273 K to final T_f=243 K. In detail, T_i

represents the maximum temperature value of brines reservoir (Zolotov, 2017) and T_f is close to the eutectic for salt-ice mixtures (245 K, see Castillo-Rogez 2018; Hesse and Castillo-Rogez, 2019). From T_i and T_f the decrement step value was ΔT= 5 K.
Exploring the possibility that the aqueous solutions freeze at different pressure conditions, in addition to the simulations carried out at 1 bar of total pressure value (as reported from literature; Zolotov, 2017), further arbitrary pressure values of 1.5 and 3 bars were considered in our models.
FREZCHEM code was initialized with molal amounts of main ions (Na, K, Ca, Mg, Cl and SO_4), as explained before, and considering the same Ceres' acidity conditions (pH=10.2) found in Zolotov (2017).
First, we calculated the amount of solid phases (salts and water ice expressed in moles) that precipitated, from the initial solutions, during each step of decreasing temperature. Then, we compared the results of the applied code with our chemical equilibria calculations to understand the equilibrium state for each precipitated mineral, during the cooling process, related to concentrations and activities of solutes, the ionic strength and density of solutions.

3 Results

3.1 Solids precipitation from initial aqueous solutions

Figs. 3 and 4 show the results derived from the cooling simulations applied to aqueous solutions in Kupalo (Fig. 3) and Juling (Fig. 4) craters at three different pressure conditions. In detail, the amounts of the solids, expressed in moles, were calculated starting from the initial water content of 1000 g at T_i=273 K decreasing to 0.1 g at the eutectic final temperature, that here was >250 K (in both cases the code stopped before the simulations arrive to the chosen T_f value).
In Figs. 3 and 4, the main vertical axis is referred to the moles number (up to 1) of all solids formed at each decrement interval of temperature excluding water ice amounts, up to 50 moles, plotted in the secondary vertical axis.
First considerations revealed that lower temperature (Figs. 3 and 4) and elevated salinity (considering water content decreasing from 1000 to 0.1 g) cause salts precipitation. The formation of water ice occurred at T=268 K (in line with results given by Zolotov, 2017 that reported the ice formation at T<270 ± 2 K) and its concentration exponentially decreased for lower temperature (blue dashed curves in Figs. 3 and 4) affecting the ionic strength of remaining solution, as further explained.
$MgCO_3$, $CaCO_3$ and $CaMg(CO_3)_2$ were the first solids to precipitate (before water ice formation) from solutions at the different total pressure values (Figs. 3 and 4). As regards hydrated Na carbonate (black dots in Figs. 3 and 4), in Kupalo, natron ($Na_2CO_3 \cdot 10H_2O$) can form simultaneously (Fig. 3b) or before (Fig. 3a and c) water ice formation. Instead, in Juling simulations, natron can precipitate only after water ice formation (Fig. 4a, b, c).
This suggests that the formation of hydrated Na-carbonates was favored in sodium-enriched solutions (e.g., in Kupalo); instead, Ca-Mg-carbonates are more favored in sodium-depleted solutions (e.g., in Juling).
About sulphated species, in our simulations, while $Na_2SO_4 \cdot 10H_2O$ formed at T=268 K in all our simulations (Figs. 3 and 4); instead, K_2SO_4 can form at lower temperatures ($T \leq 268$ K).

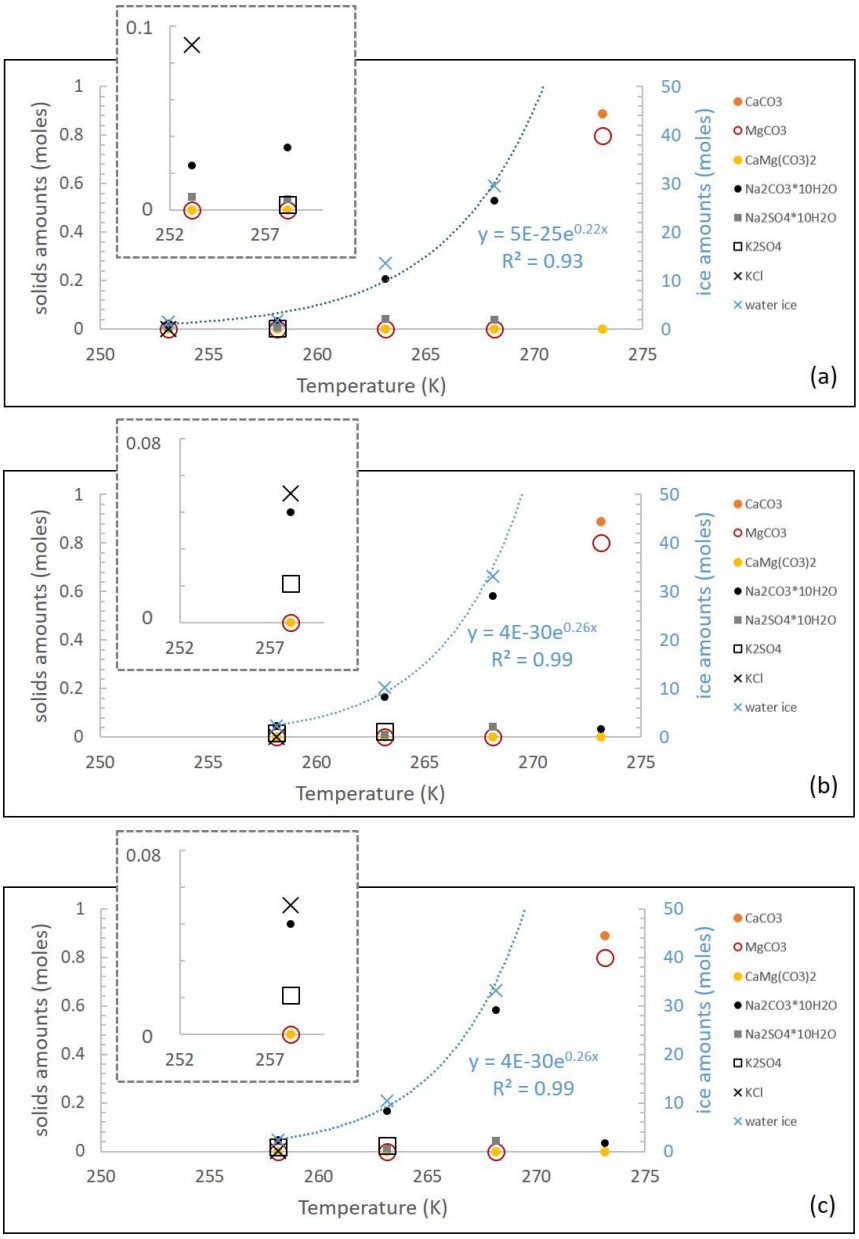

Figure 3. Results deriving from the cooling simulations applied to aqueous solutions under Kupalo crater at three different pressure conditions: (a) 1 bar, (b) 1.5 bars, and (c) 3 bars. The amounts of the solids, expressed in moles, were calculated starting from the initial water content of 1000 g at T_i=273 K decreasing to 0.1 g at the eutectic final temperature. The solids precipitated at the final temperature (T <260 K) are more clearly given in the plots enclosed in the grey dashed boxes. The main y-axis is referred to the moles number (up to 1) of all solids that formed at each decrement interval of temperature (5 K) excluding water ice amounts, up to 50 moles, plotted in the secondary y-axis (in blue). Water ice is characterized by an exponential decrement (dashed blue curve). See text for detailed explanation.

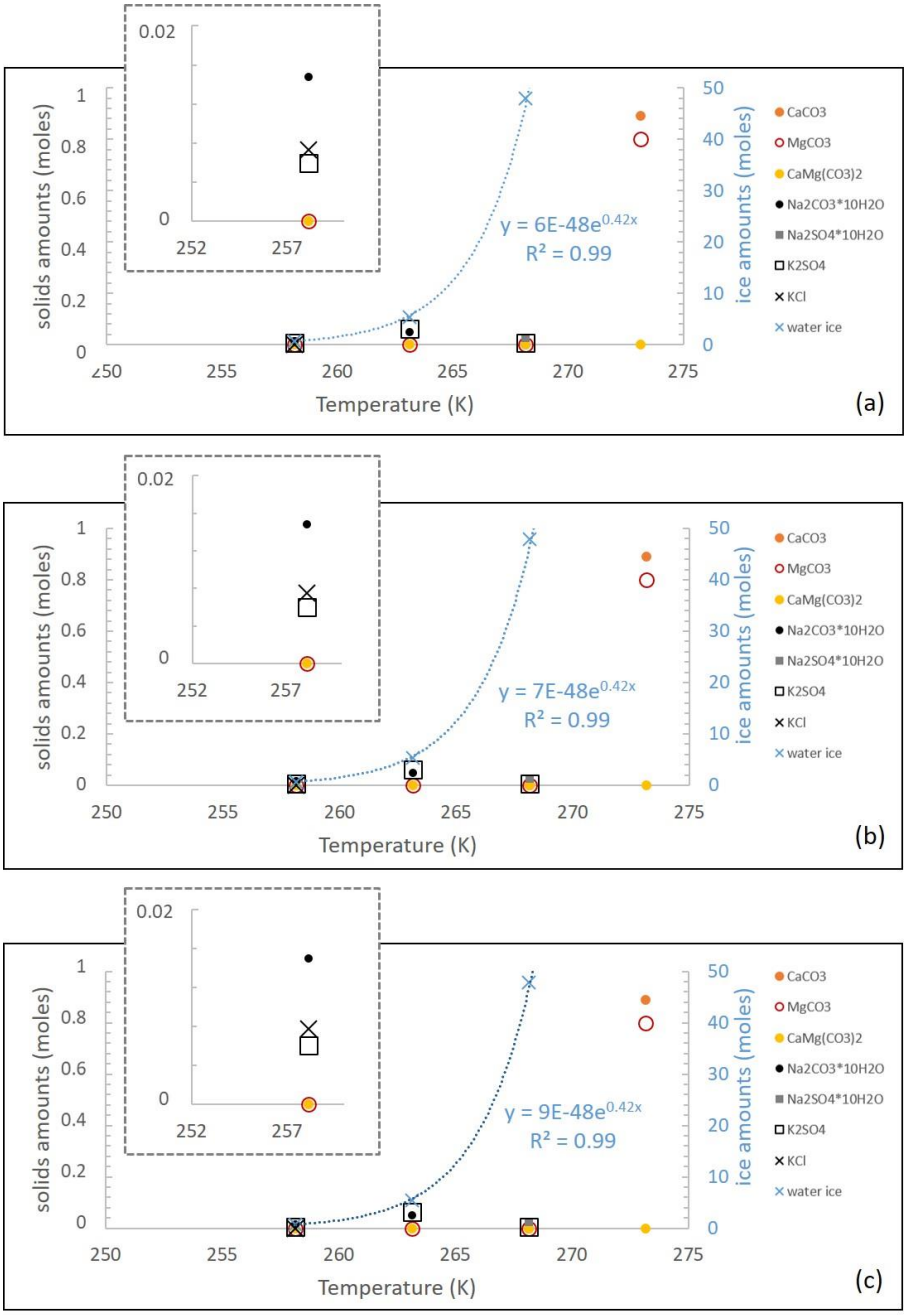

Figure 4. Results deriving from the cooling simulations applied to aqueous solutions under Juling crater at three different pressure conditions: (a) 1 bar, (b) 1.5 bars, and (c) 3 bars. The amounts of the solids, expressed in moles, were calculated and shown as expressed in Fig. 3.

At about T≤252-257 K (Fig. 3), liquid water content was <0.1 g and no more calculations could be made by the code. In that condition, at Kupalo, at 1 bar of total pressure, FREZCHEM returned that in sodium enriched solutions (for which the code runned up to lower temperatures, Fig. 3a) at 248<T<253 K precipitated solids were $NaCl{\cdot}2H_2O$ (hydrohalite) and $NaHCO_3$

(nahcolite). Instead, they did not form in simulations carried out for pressure >1 bar, and they never appeared in freezing models of Juling solutions.

Our results are in line with Thomas et al. (2019) that demonstrated that hydrohalite deposits from brines at T<251.6 K from Na-enriched solutions. In addition, we confirm that, at 1 bar of total pressure, hydrohalite can precipitate from solutions in which both Na and Cl are abundant (e.g., Na=1.8 and Cl=0.1 molal concentrations). In fact, in replicating our simulation for a solution Na-enriched but Cl-depleted (e.g., Na=1.8 and Cl=0.04 molal concentrations) we observed that $NaCl{\cdot}2H_2O$ did not precipitate, not even at 1 bar of total pressure. Moreover, $NaCl{\cdot}2H_2O$ and $NaHCO_3$ formation suggested that both solids formed under slow-kinetic (slow-freezing) processes (Vu et al., 2017) that, plausibly, could be typical processes occurring in Kupalo rather than in Juling.

In other word, carbonates are stable solids and formed in all the simulations. As regards Na-compounds, natron is favored in high Na-content environments; $NaHCO_3$ and $NaCl{\cdot}2H_2O$ are strongly pressure condition governed. In fact, $NaHCO_3$ and $NaCl{\cdot}2H_2O$ formation can occur at P=1 bar and, as suggested by Thomas et al. (2019), they can precipitate under a narrow set of conditions of slow freezing rate.

$NaCl{\cdot}2H_2O$ and $NaHCO_3$ directly participate in the acid-base equilibria in aqueous solutions with CO_2 (Anabaraonye et al., 2019) promoting pH increasing (Li et al., 2018) and influencing the dissolution/precipitation rate of carbonates. It can be noted that hydrohalite can be detected on Ceres' surface, but after its formation, in such conditions, it can be transformed into anhydrous NaCl. Anhydrous sodium chloride is IR inactive and not detectable in IR spectroscopy.

Finally, natrite (Na_2CO_3), found in Kupalo's surface layers (Carrozzo et al., 2018), could be directly formed from the hydrated natron ($Na_2CO_3{\cdot}10H_2O$) at total pressure ≥1 bar; or, alternatively, it can be derived at P=1 bar from nahcolite ($NaHCO_3$) according the following reaction:

$$2NaHCO_3 \rightarrow Na_2CO_3 + H_2O + CO_2. \qquad \text{Eq. (5)}$$

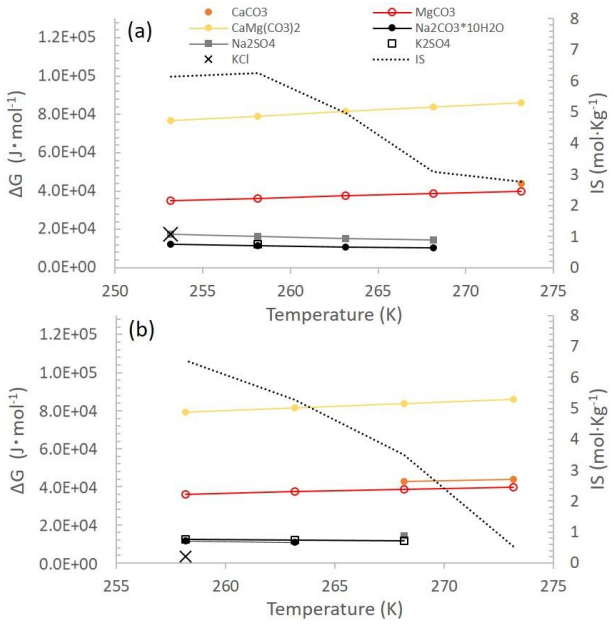

Figure 5. ΔG (the Gibbs free energy) calculated at each ΔT temperature decrement for Kupalo (a) and Juling (b) at 1 bar of total pressure. ΔG is given in $J \cdot mol^{-1}$ and for ΔG>0 solids precipitation is favored from aqueous solutions. In the same plots also IS values (the ionic strength of solutions; dotted curves) are given and expressed in $mol \cdot kg^{-1}$.

3.2 Stability in the solids-solutes equilibria

As shown in Figs. 3 and 4, in all the simulations, decreasing temperature caused the precipitations of carbonates, at first, followed by the formation of sulphates and, later, of Cl-bearing salts (KCl) from more saline brines. Only hydrated-Na-carbonate exceptionally formed after sulphates (Fig. 4) in Juling.

The calculated Gibbs free energy values (ΔG> 0, ranged from $3.4 \cdot 10^3$ to $7.9 \cdot 10^4$ $J \cdot mol^{-1}$) for the salts precipitating from the initial solutions are shown in Fig. 5 and calculated as follows:

$$\Delta G = - [\log (k_{sp}) \cdot 2.303 \cdot R \cdot T] \quad \text{Eq. (6)}$$

where T is temperature expressed in Kelvin at 5 K intervals, R is universal constant ($R = 8.3$ $J \cdot K^{-1} \cdot mol^{-1}$), k_{sp} is the equilibrium constant given from FREZCHEM code's output. The quantity k_{sp} is defined as a "solubility product" that is the product of the solutes' activities, at equilibrium, in which a solid dissociates in solutes

$$k_{sp} = [a_i]^n_{eq} \cdot [a_j]^m_{eq} \quad \text{Eq. (7)}$$

where *a* is the activity for each (i-j)-dissolved ionic species, *n* and *m* are stoichiometric parameters. The k_{sp} parameter has the same formula of IAP (Ionic Activity Product), but the latter refers to the *measured* (different from the ideal condition at equilibrium) activities. As shown in Fig. 6, k_{sp} values in the dissociation-precipitation equilibria of $MgCO_3$ and $CaMg(CO_3)_2$ followed a power law distribution and in most of cases (also for calcite) k_{sp} coincided with IAP values: that is, the solutions are saturated respect to the minerals. In that condition of saturation, the aqueous solution contains the maximum concentration of dissolved solute, compatibly with its solubility limit, and therefore it is no longer possible to dissolve other solute without minerals precipitating.

In all the reactions solid precipitation is thermodynamically favorited (ΔG>0), and the aqueous solutions are oversaturated respect to the mineral when $IAP > k_{sp}$. However, in our simulations, a particular case was represented by dolomite ($CaMg(CO_3)_2$). Compared to the other solids, dolomite showed the highest ΔG values (Fig. 5a, b) that means that it is thermodynamically favored, more than the other minerals, in both craters.

However, at Kupalo, the aforementioned IAP and k_{sp} values in the reaction involving the precipitation of dolomite showed some differences (Fig. 6a and b). The solutions were already oversaturated for dolomite at 273 K ($IAP > k_{sp}$; Fig. 6). While, at higher pressure (Fig. 6b) the solutions were saturated at T<270 K ($IAP = k_{sp}$); instead, under shallower conditions (1 bar; Fig. 6a), the saturation is not verified and dolomite (as Mg carbonate) seems less stable as solid. Possibly, under Kupalo, at a shallower depth, some processes, that directly involve other species, such as sodium, are more relevant and the solutions are less saturated for dolomite (and more saturated for natron).

Under Juling (not shown here) no differences were found with pressure and, similarly to Fig. 6b, for dolomite, $IAP > k_{sp}$ at relatively higher temperature values and $IAP = k_{sp}$ at lower temperatures.

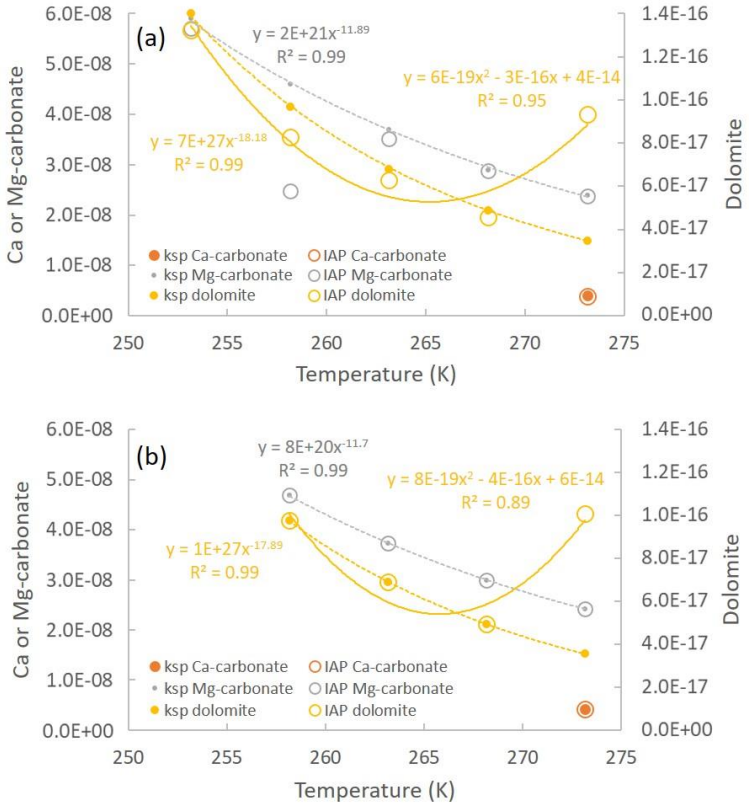

Figure 6. Comparison between equilibrium k_{sp} values and measured IAP for reactions involving the precipitation of $CaCO_3$ (orange symbols), $MgCO_3$ (grey symbols) and $CaMg(CO_3)_2$ (yellow symbols). The plot referred to Kupalo aqueous solutions at 1 bar (a) and 1.5 bars (b). At higher pressure (b), the solutions were already oversaturated for dolomite at 273 K ($IAP>k_{sp}$) and saturated at T<270 K ($IAP=k_{sp}$). Instead, under shallower conditions (a), for T<270 K, the oversaturation is not verified and dolomite (as Mg carbonate) seems less stable as solid.

4 Discussions

4.1 Implications for upwelling of aqueous solutions

The next considerations are important to explore dynamics associated with the transport of brines in conduit and fractures induced by crystallization of reservoir. First, solids precipitation feeds the cooling process, occurring under the studied craters, changing the aqueous solutions' density and viscosity.

By using FREZCHEM code, Kupalo and Juling solutions' densities (ρ_s) were calculated and the average densities were 1150 and 1130 kg·m^{-3}, respectively. This implies that density values (which average is 1140 kg·m^{-3}) are lower than crust density (1300 kg·m^{-3}; Ermakov et al., 2017) so that brines ascent could be the first way of carbonate-rich material transport to the surface. In order to understand aqueous solutions' transport dynamics and speed (v) during upwelling, we could consider the velocity (v) as a function of solutions' densities (ρ_s), the viscosity (η_w), the Reynolds number (Re) and the radius of conduit (R^*) as follows:

$$v = \frac{Re \cdot \eta_w}{\rho_s \cdot R^*} \quad \text{Eq. (8)}$$

where R^* is the radius of a cylindrical conduit, geometrically supposed to be smaller (R^*=1000 m) than the actual craters' radius (13 and 10 km for Kupalo and Juling, respectively; Stein et al., 2019). This choice is compatible with the fact that vents are larger than the underlying feeding conduits (Wilson and Head, 2017) and because large conduits may not be structurally possible (Miyamoto et al., 2005; Quick and Marsh, 2016).

As regards viscosity value, recently, Fu et al. (2017) estimated the upper layer viscosity of ~10^{20} Pa·s, in line with the fact that viscosity increases rapidly with decreasing temperature (Zolotov, 2020) and with the thermal gradient of 0.5-2 K·km^{-1} (Zolotov, 2020). In Eq. 8, certainly, we cannot give to η_w (the low-crystallized solutions viscosity) the same viscosity value found for the upper layer (Fu et al., 2017). Instead, we can assume that the viscosity (η_w) is higher than pure water viscosity known at 300 K ($8 \cdot 10^{-4}$ Pa·s), because aqueous solutions are colder and, distinctly, more saline. Moreover, at the beginning of the cooling processes, η_w can be lower than the viscosity value given for the final stage of cryolavas (~10^2 Pa·s; Quick et al., 2019) when brine has almost arrived in superficial fractures of the craters. Thus, arbitrarily, we imposed η_w ranged 1-10 Pa·s.

According to flux regime in the conduit, we can assume that a laminar flux regime (Re<1000) is maintained in the conduit up to the surface; thus, the calculated transport speed v =$8.7 \cdot 10^{-5}$ m/s from Eq. (8) results in line with velocities found at surface.

In fact, according to Quick et al. (2019), brines enriched in chloride salts would have arrived at the surface at "warm" enough temperatures to erupt travelling at least 10^{-5} m/s.

Thus, it is possible that, at first, low crystallized (with low viscosity) solutions have travelled in a conduit of radius R^*=1 km at velocities of v =$8.7 \cdot 10^{-5}$ m/s under a laminar flow regime.

During crystallization, a pressurization, induced by brine's density and viscosity variation, led to "brine expulsion" as mentioned in Hunke et al. (2011). Moreover, the convection of salty fluid allows additional solidification, which increases the solid fraction (Wettaufler et al., 1997) so that the process could become self-sustaining. As proposed by Quick et al. (2019), an over-pressure ($\Delta P/D$) of 56 Pa/m can facilitate the brines upwelling in 10 m wide fractures close to surface layers. At surface, an ascent speed of $8.4 \cdot 10^{-5}$ m/s may be derived considering gravity acceleration (g) of 0.28 m/s^2, crust density (ρ_c) of 1300 kg/m^3 (Ermakov et al., 2017), brines density (ρ_b) of 1140 kg/m^3, and the dynamic viscosity (μ) given in Quick et al. (2019), as follows:

$$v = \left[\left(\rho_c - \rho_b\right)g + \frac{\Delta P}{D}\right]\frac{R^2}{3\mu}. \quad \text{Eq. (9)}$$

For comparison, brines' velocity is seven orders of magnitude lower than gases escaping rate from clathrates decomposition (Ruesh et al., 2019). Transport speed values induced by gas expansions is beyond the purpose of our work, but, as better explained in the next paragraph, it may be an additional element facilitating anhydrous Na carbonate upwelling considering its density of 2540 kg/m^3 (Ruesch et al., 2019 and references therein).

4.2 Implications for gas-driven transport

So far, it has been shown that upwelling is triggered by freezing and crystallization process, low crystallinity and low viscosity conditions make possible brines upwelling. Then, when solid

fraction increase, another driving force may occur. For example, gas emission may be another possible way of bringing carbonate-rich materials to surface (Ruesch et al., 2019). In fact, during ascent, brines can be subject to fragmentation by expansion of gas bubbles (e.g., CO_2) contained in clathrates (Ruesch et al., 2019) that are unstable with respect to a low pressure in a permeable regolith and decompose irreversibly (Zolotov, 2020) via decompression.

With the purpose of investigating this process in the future, for all gaseous species, in this work we extrapolated the CO_2 solubility (in mol/kg of water) in carbonate particles, which move upward with ice and brines. CO_2 solubility is inversely correlated to the concentration (c) of aqueous solutions, that is our derived ionic strength, and, as expected, it decreases in shallower pressure conditions. Then, during freezing, increasing ionic strength values, led to decreasing CO_2 solubility so that the gas-driven transport is favored.

The correlation between CO_2 solubility (mol/kg) and solution concentration (c, expressed in mol/kg), at fixed values of temperature and pressure, is shown in Fig. 7, where the y-axis indicates log $[S_0/S_c]$, derived by Eq. (10):

$$\log \frac{S_0}{S_c} = K \cdot \mathrm{c} \text{ , [at T=273 K]} \qquad \text{Eq. (10)}$$

with S_0 representing CO_2 solubility in pure water (S_0=0.0686 mol/kg at P=1 bar and S_0=0.3368 mol/kg at P=5 bars; Duan and Sun, 2003) and S_c the CO_2 solubility in aqueous solution of *c* concentration (x-axis in Fig. 7). For higher concentration values of the aqueous solutions (already for *c*>1 mol/kg; Fig. 7), the solubility of the gas is more affected by depth (see the curves derived for different pressure conditions in Fig. 7). Plausibly, therefore, the gas-driven transport of brines is more effective at surface, especially for high-density Na carbonates ejecta. In other words, considering the high density of such sodium carbonates in anhydrous state (>2000 kg/m^3; Ruesch et al., 2019) the presence of dissolved gas in brines could facilitate the solids fragmentation and, if anhydrous phases are formed, these would more easily reach the surface.

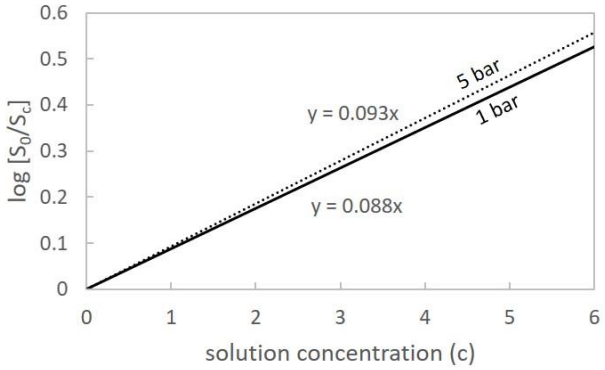

Figure 7. Plot showing the correlation between CO_2 solubility (mol/kg) and solution concentration (c, expressed in mol/kg). Here, the y-axis log $[S_0/S_c]$ is derived by Eq. (10) in the text. For higher concentration values of the aqueous solutions (already for *c* >1 mol/kg), the solubility of the gas is greater affected by depth. The correlation of Eq. 10 are given for two pressure values: 1 and 5 bars.

4.3 Salinity-Temperature dependence

In our study, the simulations returned that, during the freezing process, ionic strength (*IS*) of aqueous solutions increased up to 6.5 mol·kg^{-1} (as shown in Fig. 5). The maximum ionic strength increase, from 0.5 to 3.5 mol·Kg^{-1}, was found in Juling (Fig. 5a) in temperature values ranging between 273 and 268 K.

Between the first temperature value, corresponding to the Ca-Mg carbonates precipitation, and the latter, in which also ice and $Na_2SO_4 \cdot 10H_2O$ were formed from the initial solutions, the salinity (S, expressed in g/kg) can be derived from the following relationship:

$$T = -0.00575S + 1.710523 \cdot 10^{-3} S^{1.5} - 2.154996 \cdot 10^{-4} S^2 \quad \text{Eq. (11)}$$

in which the salinity (S) can increase up to two orders of magnitude (hundreds of g/kg). The Eq. (11) correlates the freezing temperature (in °C) and salinity (in g/kg) of an aqueous solution, then, creating a salinity-temperature line which can interpolates Ceres' brines.

For comparison, it is noted that the salinity of standard Earth seawater is ~35 g/kg and its freezing temperature is at -1.9 °C.

In our system, under Juling, if only Ca-Mg-carbonates were formed at 273 K, the salinity would be almost zero and the low density (~1000-1100 kg/m^3; calculated by FREZCHEM code) would be enough to rise the carbonates to surface even without gases-mediated transport. Moreover, Juling brines would rise under quick ascent kinetics that would distinguish it from nearby Kupalo.

On the other hand, under Kupalo, an increase in salts (NaCl) may determine a more thorough and slow cooling process, which induces a strong increase in salinity. Kupalo's brines, highly saline but still not very dense (ρ_b up to ~1200 kg/m^3) could arrive to freeze to lower temperature and could rise through the crust. Surface conditions could guarantee the formation and ejection of anhydrous-sodium-salts. On the other hand, it is conceivable that minerals formed at high salinity condition become encapsulated in the pores of the ice.

In the future, the correlation between salinity of solutions, temperature and porosity of grains may be validated by laboratory experiments carried out by using synthetic ice-salts-mixtures.

5 Conclusions

Many observations and models suggest that Ceres may have once harboured an ocean at shallow depth (Castillo-Rogez and Mc Cord, 2010), and a portion of that may still exist today as localized reservoirs (Neveu and Desch, 2015; Quick et al., 2019 and references therein) that could exist at 45 km of depth beneath Ceres' surface (Castillo-Rogez and Mc Cord, 2010). As in Occator, the proximity of Ceres' bright spots with fractured morphologies and craters, could be indicative of subsurface conduits that facilitated aqueous solutions upwelling (Quick et al., 2019) and, in many cases, effusive and explosive volatile-driven eruptions (De Sanctis et al., 2016; Nathues et al., 2017; 2019; Ruesch et al., 2019). An excess of pressure in the reservoir, after gradual freezing, could have supported an intrusion of briny materials to Ceres' surface, similarly to processes on the icy satellites of the outer solar system (Fagents, 2003; Manga and Wang, 2007).

In this work, we started assuming that the Ceres' reservoir has had an initial temperature of 273 K and is characterized by a mixture of chloride and sodium carbonate brines (Zolotov, 2017). We used FREZCHEM code to simulate the cooling process of brines from initial temperature of 273 K to see what kind of solids can precipitate during brines re-frozen under Ceres' surface. In

particular, we selected two geologically young craters hosting some of the brightest and most extensive carbonates rich areas (Carrozzo et al., 2018; De Sanctis et al., 2019).

The first aim was to understand if their different compositions in terms of different carbonates (detected at surface with VIR spectral analysis) reflect different speciation and differentiation of the initial aqueous solutions feeding both craters. Actually, we found that the different composition can be explained if the initial aqueous solutions under Juling and under Kupalo had different chemical speciation (detailed in Tab. 2). They are plotted in Langelier-Ludwig diagram (Fig. 2) and, possibly, may freeze at different P-T conditions.

During the freezing process, solids precipitation occurred in temperature values above the eutectic (245 K) for salts-ice mixtures. $MgCO_3$, $CaCO_3$ and $CaMg(CO_3)_2$ were the first solids to precipitate (before water ice formation) as shown in Figs. 3 and 4.

The formation of hydrated Na carbonate (natron $Na_2CO_3 \cdot 10H_2O$) is highly favored in Na-enriched solution (e.g., Kupalo); instead, natron could form only after water ice precipitation in Na-depleted solutions (e.g., in Juling).

Sodium bicarbonate ($NaHCO_3$) is considered as possible constituents of brines (De Sanctis et al., 2016; Zolotov, 2017; Castillo-Rogez et al., 2018). Thomas et al. (2019) suggested that it forms under slow freezing process. According to our simulations, together with hydrohalite, it can form under a narrow set of conditions (from bicarbonate alkaline aqueous solutions at P=1 bar) and we can suppose that its formation is pressure governed.

Hydrohalite itself could be detected in VIR range (0.25-5.0 μm; De Sanctis et al., 2011). However, since the hydrated compounds are not stable on the surface of Ceres (Zolotov, 2017), hydrohalite can dehydrate into NaCl, which is inactive in VIR range of sensitivity.

Some molecules which generally form under fast freezing conditions, as NH_4Cl (Thomas et al., 2019), was not detected in Kupalo crater (Carrozzo et al., 2018) in support of our hypothesis that definitively exclude fast freezing of its brines.

Our simulations confirm the endogenous origin of solid compounds observed on Ceres'surface. These solids formed during the brines freezing in the subsurface and, possibly, in terms of salinity, density, and volatiles solubility, these brines reached the surface from below.

New models (Buczkowski et al., 2018) suggested that some of craters' fractures might have formed due to a solid-state flow of a low-viscosity and low-density material intruding beneath the craters. Certainly, in our estimates, the aqueous solutions could have densities of 1140 ± 10 kg/m^3 and they could move upward in a cylindrical conduit with a presumed radius (R^*) of 1 km. After crystallization, an over-pressure can facilitate the brines upwelling, in 10 m wide fractures in which an ascent speed of about $8 \cdot 10^{-5}$ m/s was calculated, fracturing the floor-craters (catalogued in Buczkowski et al., 2018) at surface. About viscosity of aqueous solutions, it may be supposed that it increases during crystallization from the initial value ranged 1-10 Pa·s up to values found by Quick et al. (2019) for cryolavas.

Our models suggested that Na-Cl-enriched solutions could freeze at a lower temperature with respect to Na-Cl-depleted solutions. Moreover, because temperatures are inversely correlated with salinity values (Eq. 11), it cannot be excluded that Kupalo brines have freezed, reaching temperatures lower than Juling, becoming more saline. In a high-salinity and high ionic strength condition, under shallower layers, gases escaping is more favored so that the gas-driven transport may be more decisive for bringing high-density solids (as sodium carbonate particles) to the surface.

Natrite (Na_2CO_3) was found in Kupalo's surface layers and its formation is debated. It could have been directly formed from the hydrated natron and nahcolite ($Na_2CO_3 \cdot 10H_2O$ and $NaHCO_3$

respectively) at 1 bar of total pressure; or, alternatively, at pressure >1 bar, natrite (Na_2CO_3) could only derive from dehydration of natron ($Na_2CO_3 \cdot 10H_2O$).
Finally, since hydrated ammonia salts, as NH_4Cl or NH_4HCO_3 are not found to form preferentially, with respect to sodium salts, even in ammonium-dominated solutions (Vu et al., 2017), we have deliberately neglected to investigate the role of ammonia. The detection of NH_4Cl may imply an early subsurface reservoir rich in ammonium and/or chloride, and for future investigations, we will focus on the processes in which ammonium and sodium could be featured.
Understanding deeper into the freezing processes within the Solar System will be an important step for future investigations.

Acknowledgments

This research was funded by Agenzia Spaziale Italiana and supported by the *Dawn* VIR team at INAF-IAPS in Rome, Italy.
Data deriving from the mission *Dawn* are available at repository PDS (Planetary Data System) at url: https://sbn.psi.edu/pds/resource/dawn/dwncvirL1.html and also https://sbib.psi.edu/data/PDS-Ceres/about.html. FREZCHEM code is free and available at url: https://www.dri.edu/frezchem. All authors accepted the manuscript.

References

Ammannito, E., M. C. DeSanctis, M. Ciarniello, A. Frigeri, F. G. Carrozzo, J.-Ph. Combe, B. L. Ehlmann, S. Marchi, H. Y. McSween, A. Raponi, M. J. Toplis, F. Tosi, J. C. Castillo-Rogez, F. Capaccioni, M. T. Capria, S. Fonte, M. Giardino, R. Jaumann, A. Longobardo, S. P. Joy1, G. Magni, T. B. McCord, L. A. McFadden, E. Palomba, C. M. Pieters, C. A. Polanskey, M. D. Rayman, C. A. Raymond, P. M. Schenk, F. Zambon, and C. T. Russell (2016), Distribution of phyllosilicates on the surface of Ceres, Science, 353(6303), doi:10.1126/science.aaf4279.

Anabaraonye, B. U., J. P. Crawshaw, and J. P. M. Trusler (2019), Brine chemistry effects in calcite dissolution kinetics at reservoir conditions, Chemical Geology, 509, 92–102, doi:10.1016/j.chemgeo.2019.01.014.

Beck, P., B. Schmitt, E. Cloutis, and P. Vernazza (2015), Low-temperature reflectance spectra of brucite and the primitive surface of 1-Ceres?, Icarus, 257, 471–476, doi:10.1016/j.icarus.2015.05.031.

Buczkowski, D. L., H. G. Sizemore, M. T. Bland, J. E. C. Scully, L. C. Quick, K. H. G. Hughson, et al. (2018), Floor-fractured craters on Ceres and Implications for interior processes, Journal of Geophysical Research: Planets, 123, 3188–3204, https://doi.org/10.1029/2018JE005632.

Carrozzo, F. G., M. C. De Sanctis, A. Raponi, E. Ammannito, J. Castillo-Rogez, B. L. Ehlmann, S. Marchi, N. Stein, M. Ciarniello, F. Tosi, F. Capaccioni, M. T. Capria, S. Fonte, M. Formisano, A. Frigeri, M. Giardino, A. Longobardo, G. Magni, E. Palomba, F. Zambon, C. A. Raymond,

695 and C. T. Russell (2018), Nature, formation, and distribution of carbonates on Ceres, Sci. Adv.,
696 4(3), doi:10.1126/sciadv.1701645.
697
698 Castillo-Rogez, J. C., and T. B. McCord (2010), Ceres' evolution and present state constrained
699 by shape data, Icarus, 205(2), 443–459, doi:10.1016/j.icarus.2009.04.008.
700
701 Castillo-Rogez, J. C. (2011), Ceres - Neither a porous nor salty ball, Icarus, 215(2), 599–602,
702 doi:10.1016/j.icarus.2011.08.007.
703
704 Castillo-Rogez, J. C., M. Neveu , H. Y. McSween, R. R. Fu, M. J. Toplis, and T. Prettyman
705 (2018), Insights into Ceres's evolution from surface composition, Meteoritics and Planetary
706 Science, https://doi.org/10.1111/maps.13181.
707
708 Ciarniello, M., M. C. De Sanctis, E. Ammannito, A. Raponi, A. Longobardo, E. Palomba, F. G.
709 Carrozzo, F. Tosi, J.-Y. Li, S. E. Schröder, F. Zambon, A. Frigeri, S. Fonte, M. Giardino, C. M.
710 Pieters, C. A. Raymond, and C. T. Russell (2017), Spectrophotometric properties of dwarf planet
711 Ceres from the VIR spectrometer on board the Dawn mission, Astronomy & Astrophysics, doi:
712 10.1051/0004-6361/201629490.
713
714 De Sanctis, M. C., A. Coradini, E. Ammannito, G. Filacchione, M. T. Capria, S. Fonte, G.
715 Magni, A. Barbis, A. Bini, M. Dami, I. Ficai-Veltroni, and G. Preti (2011), The VIR
716 spectrometer, Space Sci. Rev., 163, 329–369.
717
718 De Sanctis, M. C., E. Ammannito, A. Raponi, S. Marchi, T. B. McCord, H. Y. McSween, F.
719 Capaccioni, M. T. Capria, F. G. Carrozzo, M. Ciarniello, A. Longobardo, F. Tosi, S. Fonte, M.
720 Formisano, A. Frigeri, M. Giardino, G. Magni, E. Palomba, D. Turrini, F. Zambon, J.-P. Combe,
721 W. Feldman, R. Jaumann, L. A. McFadden, C. M. Pieters, T. Prettyman, M. Toplis, C. A.
722 Raymond, and C. T. Russell, (2015) Ammoniated phyllosilicates with a likely outer Solar
723 System origin on (1) Ceres, Nature, 528, 241–244.
724
725 De Sanctis, M. C., A. Raponi, E. Ammannito, M. Ciarniello, M. J. Toplis, H. Y. McSween, J. C.
726 Castillo-Rogez, B. L. Ehlmann, F. G. Carrozzo, S. Marchi, F. Tosi, F. Zambon, F. Capaccioni,
727 M. T. Capria, S. Fonte, M. Formisano, A. Frigeri, M. Giardino, A. Longobardo, G. Magni, E.
728 Palomba, L. A. McFadden, C. M. Pieters, R. Jaumann, P. Schenk, R. Mugnuolo, C. A. Raymond,
729 and C. T. Russell, (2016), Bright carbonate deposits as evidence of aqueous alteration on (1)
730 Ceres, Nature, 536, 54–57.
731

De Sanctis, M. C., A. Frigeri, E. Ammannito, F. G. Carrozzo, M. Ciarniello, F. Zambon, F. Tosi, A. Raponi, A. Longobardo, J. P. Combe, E. Palomba, F. Schulzeck, C. A. Raymond, and C. T. Russell (2019), Ac-H-11 Sintana and Ac-H-12 Toharu quadrangles: Assessing the large and small scale heterogeneities of Ceres' surface, Icarus, 318, 230-240, https://doi.org/10.1016/j.icarus.2017.08.014.

Duan, Z., and R. Sun (2003), An improved model calculating CO_2 solubility in pure water and aqueous NaCl solutions from 273 to 533 K and from 0 to 2000, Chemical Geology, 193, 257-271, https://doi.org/10.1016/S0009-2541(02)00263-2.

Ermakov, A. I., R. R. Fu, J. C. Castillo-Rogez, C. A. Raymond, R. S. Park, F. Preusker, C. T. Russell, D. E. Smith, and M. T. Zuber (2017), Constraints on Ceres' internal structure and evolution from its shape and gravity measured by the dawn spacecraft, J. Geophys. Res. Planets, 122, 2267-2293.

Fagents, S. A. (2003), Considerations for effusive cryovolcanism on Europa: the post Galileo perspective, J. Geophys. Res., 108, 5139, https://doi.org/10.1029/2003JE002128.

Fanale, F. P., and J. R. Salvail (1989), The water regime of asteroid 1 Ceres, Icarus, 82, 97–110.

Formisano, M., M. C. De Sanctis, G. Magni, C. Federico, and M. T. Capria (2016), Ceres water regime: surface temperature, water sublimation and transient exo(atmo)sphere, MNRAS, 455, 1892-1904, doi:10.1093/mnras/stv2344.

Fu, R, E. Ermakov, S. Marchi, J. C. Castillo-Rogez, and C. A. Raymond (2017), The interior structure of Ceres as revealed by surface topography, Earth Planet. Sci. Lett 476, 153-164.

Hayne, P.O., Aharonson, O., 2015. Thermal stability of ice on Ceres with rough topography. J. Geophys. Res. Planets 120, 1567–1584, doi:10.1002/2015JE004887.

Hesse, M. A., and J. C. Castillo-Rogez (2019), Thermal Evolution of the Impact-Induced Cryomagma Chamber Beneath Occator Crater on Ceres, Geophysical Research Letters, 46(3), 1213-1221, doi:10.1029/2018GL080327.

Hunke, E. C., D. Notz, A. K. Turner, and M. Vancoppenolle (2011), The multiphase physics of sea ice: a review for model developers, The Cryosphere, 5, 989–1009, doi:10.5194/tc-5-989-2011.

King, T. V. V., R. N. Clark, W. M. Calvin, D. M. Sherman, and R. H. Brown (1992), Evidence for ammonium-bearing minerals on Ceres, Science, 255(5051), 1551-1553, doi:10.1126/science.255.5051.1551.

Langelier, W. F., and H. F. Ludwig (1942), Graphical Methods for Indicating the Mineral Character of Natural Waters, Journal (American Water Works Association), 34(3), 335–352.

Lebofsky, L. A., M. A. Feierberg, A. T. Tokunaga, H. P. Larson, and J. R. Johnson (1981), The 1.7- to 4.2-μm spectrum of asteroid 1 Ceres: Evidence for structural water in clay minerals, Icarus, 48(3), 453–459, doi:10.1016/0019-1035(81)90055-5.

Li, J.-Y., L. A. McFadden, J. W. Parker, E. F. Young, S. A. Stern, P. C. Thomas, C. T. Russell, and M. V. Sykes (2006), Photometric analysis of 1 Ceres and surface mapping from HST observations, Icarus, 182(1), 143–160, doi:10.1016/j.icarus.2005.12.012.

Li, J.-Y., S. E. Schröder, S. Mottola, A. Nathues, J. C. Castillo-Rogez, N. Schorghofer, D. A. Williams, M. Ciarniello, A. Longobardo, C. A. Raymond and C. T. Russell (2019) Spectrophotometric modeling and mapping of Ceres, Icarus, 322, 144-167, https://doi.org/10.1016/j.icarus.2018.12.038.

Li, X., C. Peng, J. P. Crawshaw, G.C. Maitland, and J. P. M. Trusler (2018), The pH of CO_2-saturated aqueous NaCl and $NaHCO_3$ solutions at temperatures between 308 K and 373 K at pressures up to 15 MPa, Fluid Phase Equilibria, 458, 253–263.

Manga, M., and C. Y. Wang (2007), Pressurized oceans and the eruption of liquid water on Europa and Enceladus, Geophys. Res. Lett., 34, L07202.

Marion, G.M., and S. A. Grant (1994), A chemical-thermodynamic model for aqueous solutions at subzero temperatures, CRREL Spec. Rpt., 94-18, Hanover, NH.

Marion, G. M., D. C. Catling, and J. S. Kargel (2003), Modeling aqueous ferrous iron chemistry at low temperatures with application to Mars, Geochim. Cosmochim. Acta, 67, 4251–4266.

Marion, G. M., M. V. Mironenko, and M. W. Roberts (2010), FREZCHEM: A geochemical model for cold aqueous solutions, Computers & Geosciences, 36(1), 10–15, https://doi.org/10.1016/j.cageo.2009.06.004.

McCord, T. B., and C. Sotin (2005), Ceres: Evolution and current state, J. Geophys. Res., 110, E05009, doi:10.1029/2004JE002244.

McSween, H. Y., J. P. Emery, A. S. Rivkin, M. J. Toplis, J. C. Castillo-Rogez, T. H. Prettyman, M. C. De Sanctis, C. M. Pieters, C. A. Raymond, and C. T. Russell (2017), Carbonaceous chondrites as analogs for the composition and alteration of Ceres, Meteorit. Planet. Sci., 1–12, http://dx.doi.org/10.1111/maps.12947.

Milliken, R. E., and A. S. Rivkin (2009), Brucite and carbonate assemblages from altered olivine-rich materials on Ceres, Nat. Geosci., 2(4), 258–261, doi:10.1038/ngeo478.

Miyamoto, H., G. Mitri, A. P. Showman, and J. M. Dohm (2005), Putative ice flows on Europa: geometric patterns and relation to topography collectively constrain material properties and effusion rates, Icarus, 177, 413–424.

822 Nathues, A., T. Platz, G. Thangjam et al. (2017), Evolution of Occator Crater on (1) Ceres,
823 Astronom. J., 153(3), doi: 10.3847/1538-3881/153/3/112.
824
825 Nathues, A., T. Platz, G. Thangjam, M. Hoffmann, J. E. C. Scully, N. Stein, O. Ruesch, and K.
826 Mengel (2019), Occator Crater in Color at Highest Spatial Resolution, Icarus, 320, 24–38.
827
828 Neveu, M., S. J. Desch, and J. C. Castillo-Rogez (2015), Core cracking and hydrothermal
829 circulation can profoundly affect Ceres' geophysical evolution, J. Geophys. Res. Planets, 120,
830 123–154, doi:10.1002/2014JE004714.
831
832 Neveu, M., and S. J. Desch (2015), Geochemistry, thermal evolution, and cryovolcanism on
833 Ceres with a muddy ice mantle, Geophys. Res. Lett., 42, 10,197–10, 206,
834 doi:10.1002/2015GL066375.
835
836 Park, R. S., A. T. Vaughan, A. S. Konopliv, A. I. Ermakov, N. Mastrodemos, et al. (2019), High-
837 resolution shape model of Ceres from stereophotoclinometry using Dawn Imaging Data, Icarus,
838 319, 812-827.
839
840 Pitzer, K.S (1995), Thermodynamics, 3rd ed., McGraw-Hill, New York, 626 pp.
841
842 Postberg, F., J. Schmidt, J. Hillier, S. Kempf, and R. Srama (2011), A salt-water reservoir as the
843 source of a compositionally stratified plume on Enceladus, Nature, 474, 620–622.
844
845 Quick, L.C., and B. D. Marsh (2016), Heat transfer and cooling of ascending cryomagmas on
846 Europa, J. Volcanol. Geotherm. Res., 319, 66–77.
847
848 Quick, L. C., D. L. Buczkowski, O. Ruesch, J. E. C. Scully, J. Castillo-Rogez, C. A. Raymond,
849 et al. (2019), A possible brine reservoir beneath Occator crater: Thermal and compositional
850 evolution and formation of the Cerealia Dome and Vinalia Faculae, Icarus, 320, 119-135,
851 https://doi.org/10.1016/j.icarus.2018.07.016.
852
853 Raponi, A., M. C. De Sanctis, A. Frigeri, E. ammannito, M. Ciarniello, M. Formisano, J-P.
854 Combe, G. Magni, et al. (2018), Variations in the amount of water ice on Ceres' surface suggest
855 a seasonal water cycle, Science Advances, doi: 10.1126/sciadv.aao3757.
856
857 Raponi, A., M. C. De Sanctis, F. G. Carrozzo, M. Ciarniello, J. C. Castillo-Rogez, E.
858 Ammannito, A. Frigeri, A. Longobardo, E. Palomba, F. Tosi, F. Zambon, C. A. Raymond, and
859 C. T. Russell (2019), Mineralogy of Occator crater on Ceres and insight into its evolution from
860 the properties of carbonates, phyllosilicates, and chlorides, Icarus, 320, 83–96,
861 https://doi.org/10.1016/j.icarus.2018.02.001.
862
863 Rivkin, A. S., E. L. Volquardsen, and B. E. Clark (2006), The surface composition of Ceres:
864 Discovery of carbonates and iron-rich clays, Icarus, 185(2), 563–567,
865 doi:10.1016/j.icarus.2006.08.022.
866
867 Rivkin, A. S., J.-Y. Li, R. E. Milliken, L. F. Lim, A. J. Lovell, B. E. Schmidt, L. A. McFadden,
868 and B. A. Cohen (2012), The surface composition of Ceres, in The Dawn Mission to Minor

Planets 4 Vesta and 1 Ceres, edited by S. Redline and N. A. Berger, pp. 95–116, Springer, New York,
doi:10.1007/978-1-4614-4903-4_7.

Ruesch, O., A. Nathues, R. Jaumann, et al. (2017), Faculae on Ceres: possible formation mechanisms, Lunar Planet. Sci., 48, 2435.

Ruesch, O., L. C. Quick, M. E. Landis, M. M. Sori, O. Čadek, P. Brož, K. A. Otto, M. T. Bland, S. Byrne, J. C. Castillo-Rogez, H. Hiesinger, R. Jaumann, K. Krohn, L. A. McFadden, A. Nathues, A. Neesemann, F. Preusker, T. Roatsch,…and C. T. Russell (2019), Bright carbonate surfaces on Ceres as remnants of salt-rich water fountains, Icarus, 320, 39–48, https://doi.org/10.1016/j.icarus.2018.01.022.

Ruiz, J., A. Jiménez-Díaz, F. Mansilla, L. M. Parro, I. Egea-González, and M. Küppers (2019), Evidence of thrust faulting and widespread contraction of Ceres, Nature astronomy, https://doi.org/10.1038/s41550-019-0803-2.

Russell, C. T., and C. A. Raymond, (2011), The Dawn Mission to Vesta and Ceres, Space Sci. Rev., 163, 3-23, doi 10.1007/s11214-011-9836-2.

Russell, C.T., C. A. Raymond, E. Ammannito, D. L. Buczkowski, M. C. De Sanctis, H. Hiesinger, R. Jaumann, A. S. Konopliv, H. Y. McSween, A. Nathues, R. S. Park, C. M. Pieters, T. H. Prettyman, T. B. McCord, L. A. McFadden, S. Mottola, M. T. Zuber, S. P. Joy, C. Polanskey, M. D. Rayman, J. C. Castillo-Rogez, P. J. Chi, J. P. Combe, A. Ermakov, R. R. Fu, M. Hoffmann, Y. D. Jia, S. D. King, D. J. Lawrence, J. Y. Li, S. Marchi, F. Preusker, T. Roatsch, O. Ruesch, P. Schenk, M. N. Villarreal, and N. Yamashita (2016), Dawn arrives at Ceres: exploration of a small, volatile-rich world, Science, 353, 1008–1010.

Stein, N. T., B. L. Ehlmann, E. Palomba, M. C. De Sanctis, A. Nathues, H. Hiesinger, E. Ammannito, C. A. Raymond, R. Jaumann, A. Longobardo, and C. T. Russell (2019), The formation and evolution of bright spots on Ceres, Icarus, 320, 188–201, https://doi.org/10.1016/j.icarus.2017.10.014.

Thomas, E. C., T. H. Vu, R. Hodyss, P. V. Johnson, and M. Choukroun (2019), Kinetic effect on the freezing of ammonium-sodium-carbonate-chloride brines and implications for the origin of Ceres' bright spots, Icarus, 320, 150–158, doi:10.1016/j.icarus.2017.12.038.

Vu, T. H., R. Hodyss, P. V. Johnson, and M. Choukroun (2017), Preferential formation of sodium salts from frozen sodium-ammonium-chloride-carbonate brines – Implications for Ceres' bright spots, Planetary and Space Science, 141, 73–77.

Wettlaufer, J. S., M. G. Worster, and H. E. Huppert (1997), Natural convection during solidification of an alloy from above with application to the evolution of sea ice, Journal of Fluid Mechanics, 344, 291–316.

Wilson, L., and J. W. Head (2017), Generation, ascent and eruption of magma on the Moon: New insights into source depths, magma supply, intrusions and effusive/explosive eruptions (Part 1: Theory), 283, 146–175, https://doi.org/10.1016/j.icarus.2015.12.039.

Zambon, F., A. Raponi, F. Tosi, M. C. De Sanctis, L. A. McFadden, F. G. Carrozzo, A. Longobardo, M. Ciarniello, K. Krohn, K. Stephan, E. Palomba, C. M. Pieters, E. Ammannito, C. T. Russell, and C. A. Raymond (2017), Spectral analysis of Ahuna Mons from Dawn mission's visible-infrared spectrometer, Geophys. Res. Lett. 44, 97–104.

Zolotov, M. Yu. (2015), Physical chemistry of impact-generated fluids and bright spots on Ceres, Meteorit. Planet. Sci., 50 Suppl, Abstract 5384.

Zolotov, M. Yu. (2017), Aqueous origins of bright salt deposits on Ceres, Icarus, 296, 289–304.

Zolotov, M. Yu. (2020), The composition and structure of Ceres' interior, Icarus, 335, https://doi.org/10.1016/j.icarus.2019.113404.